OE Optical Engineering

RESEARCH PAPER

Classification of material and surface roughness using polarimetric multispectral LiDAR

Yu Han,* David Salido-Monzú, and Andreas Wieser
ETH Zurich, Institute of Geodesy and Photogrammetry, Zurich, Switzerland

ABSTRACT. Multispectral light detection and ranging (LiDAR) is an emerging active remote sensing technique that combines distance and spectroscopy measurements. The reflectance spectrum is known to enable material classification. However, the spectrum also depends on other surface parameters, particularly roughness. Herein, we propose an extension of multispectral to polarimetric multispectral LiDAR and introduce unpolarized and linearly polarized reflectance spectra as additional features for classifying materials and roughness. Using a bench-top prototype instrument, we demonstrate the feasibility and benefit of acquiring unpolarized and linearly polarized reflectance spectra. We analyze and interpret the spectra obtained with two different spectral resolutions (10 and 40 nm) from measurements on test specimens consisting of five different materials with two different levels of surface roughness. Using a linear support vector machine, we demonstrate the potential of the different features for enabling material and roughness classification. We find that the unpolarized reflectance spectrum is well suited for classifying materials, and the linearly polarized one for classifying roughness. In both cases, the performance is much better than using a standard reflectance spectrum offered by multispectral LiDAR. We identify polarimetric multispectral LiDAR as a technology that may significantly enhance surface and material probing capabilities for remote sensing applications.

Keywords: multispectral light detection and ranging; polarimetry; material classification; roughness classification; polarized reflectance spectrum; unpolarized reflectance spectrum

Paper 20230678G received Jul. 17, 2023; revised Oct. 6, 2023; accepted Nov. 7, 2023; published Nov. 21, 2023.

1 Introduction

Multispectral light detection and ranging (LiDAR) combines contactless distance measurement and remote spectroscopy. It provides three-dimensional (3D) spatial data and information about the scanned materials through their reflectance spectra. This multimodal sensing is beneficial for applications in various fields, such as remote sensing,[1] digitization of the environment,[2] autonomous driving,[3] mining,[4] and smart agriculture.[5] The material probing capability of multispectral LiDAR, however, is often impaired by different surface finishing, especially due to the impact of roughness on reflectance.[6,7] In contrast, surface roughness is itself also an important characteristic of the scanned objects.[8–11] Conventional optical techniques for independent roughness measurement, such as interferometry or confocal microscopy, are limited to small working areas. In many practical applications involving large scenes or surfaces whose roughness needs to be assessed remotely, they are thus not applicable.[12] For instance, comprehensive building information modeling (BIM) requires precise 3D geometry[13] and semantically rich material information[14] for

*Address all correspondence to Yu Han, yu.han@geod.baug.ethz.ch

as-built BIM[15] in the construction phase and as-is BIM[16] in heritage protection[17] and circular construction.[18] The impact of surface roughness weakens accurate material information extraction from the reflectance spectrum. Conversely, surface roughness information of different building components is valuable for quality control in construction[10,19] and degradation assessment of construction materials.[11,20] Therefore, decoupling the impacts of material composition and surface roughness on the reflectance spectrum measured by multispectral LiDAR is highly beneficial to extract rich and accurate material information.

Some attempts have been proposed to work around this limitation in LiDAR sensing. Previous investigations either assumed the rough target surface to be a perfectly Lambertian reflector[21] or estimated the surface roughness from the parameters of a complex reflection model determined by measuring reflectance spectra at different incidence and observation angles (angle-resolved scattering approach).[22,23] Really Lambertian surfaces, however, are rarely found in practice,[24] and the angle-resolved scattering approach is laborious and model-dependent. Polarimetry is a suitable technology that can be adapted to LiDAR sensing to enable surface roughness estimation at each measurement point. Investigations on monochromatic polarization-coded LiDAR demonstrated the relation between the degree of linear polarization (DoLP) of the backscattered light and the target surface roughness. This relation was already used for classifying highly specular car paints and certain diffuse man-made and natural targets.[25] Our previous work on a novel polarimetric multispectral LiDAR also showed the relationship between DoLP and material specularity.[26]

The physical basis for the polarimetric approaches was described and discussed by Wolff and Boult.[27] In a LiDAR system employing a linearly polarized laser source, the mechanism of light–matter interaction consists of two procedures: (1) specular reflections on the irregular surface microfacets, and (2) volume scattering of light penetrated into the target subsurface. The reflections on the surface preserve the linear polarization of the laser source, thus contributing a polarized component to the backscattered light. Conversely, the volume scattering depolarizes the penetrated light and thereby contributes an unpolarized component to the backscattered signal.

Polarimetric LiDAR incorporates polarimetry into LiDAR technology and has been extensively applied in atmospheric sensing.[28–33] A few attempts of polarimetric LiDAR focus on enhancing the detection of solid targets,[34,35] such as vegetation,[36–39] distant constructions,[40] and objects relevant to autonomous driving in low-visibility conditions.[25,41] However, established polarimetric LiDARs are only single-, dual-, or triple-wavelength, being thus largely limited in extracting surrounding material information accurately. Although passive and active spectral polarimeters[42,43] can tackle these challenges, a comprehensive 3D model with rich material information requires additional co-registration between the spectral polarimetric data and 3D geometry data acquired independently.

In this paper, we adapt polarimetry to multispectral LiDAR so that a single polarimetric multispectral LiDAR instrument combines polarimetry, active remote spectroscopy, and LiDAR. From each measurement point, the data of 3D geometry, linearly polarimetric characteristics, and multispectral reflectance (up to 33 wavelengths) can be directly obtained without any data co-registration. Furthermore, we introduce the concept of linearly polarized and unpolarized reflectance spectra along with a method to obtain them from a polarimetric multispectral LiDAR system. We demonstrate this using a lab prototype of such a system. Data obtained from 10 test specimens of different materials and roughness levels allow us to show that the unpolarized and linearly polarized reflectance spectra actually decouple the impacts of material and surface roughness, and thus improve the performance of material and roughness classification as compared to processing a standard reflectance spectrum only. Moreover, an initial analysis of the impact of the applied spectral configuration on material and roughness classification was carried out by comparing the performance of two spectral configurations with different resolutions. The LiDAR instrument also provides spectrally resolved high-precision distance measurements. Details on the measurement process, the quality, and potential use of these data, with a particular focus on distance, have been published already.[44,45] Herein, we focus exclusively on the use of the various reflectance spectra derived from the instrument's output.

The rest of the paper is structured as follows: In Sec. 2, we introduce the standard, unpolarized, and linearly polarized reflectance spectra and define the approaches to obtain them. In

addition, our experimental prototype of a multispectral LiDAR system and the upgraded polarimetric multispectral LiDAR are depicted. The investigated 10 material specimens in 5 material categories and 2 roughness levels are presented in Sec. 3, along with the method for collecting different multispectral features from these material specimens. In Sec. 4, we show and discuss the multispectral features obtained from standard and from polarimetric multispectral LiDAR in two different spectral configurations. We analyze their respective benefit for classifying material and surface roughness using a linear support vector machine (SVM).[46,47] Finally, we conclude and give a brief outlook on future work in Sec. 5.

2 Experimental Setup and Determination of Spectra

The experimental setup of the multispectral LiDAR[45] (see Fig. 1) includes a supercontinuum optical frequency comb (SC-OFC) laser source with linear polarization. The SC-OFC output transmits through one of the band-pass filters mounted in a bank of filter wheels. A portion of filtered linearly polarized laser light illuminates the target surface (specimen) 0.5 m away from the focusing element with approximately normal incidence angle. A parabolic mirror collects the light backscattered from the target and focuses it on the probing avalanche photodiode (APD). The other portion of the filtered laser beam is focused on the reference APD. The distance of the target is calculated from the phase difference of the electrical beat notes output by the two APDs.[48] Forty band-pass filters mounted in eight filter wheels provide two different spectral configurations (Fig. 2) within the spectral range of the SC-OFC. Each six-position filter wheel has five positions mounted with filters and one position empty. By rotating the filter wheels, only the corresponding band-pass filter at the selected spectral channel is in the optical path. Seven band-pass filters with 40 nm bandwidth (BW) and central wavelengths from 600 to 900 nm

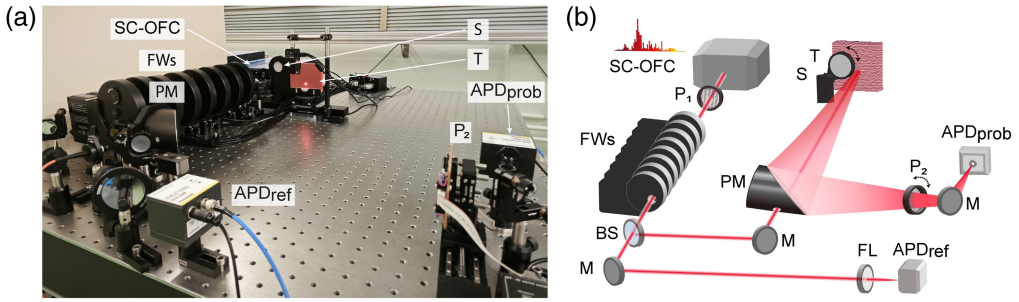

Fig. 1 Experimental setup. (a) Picture of the experimental setup (SC-OFC, supercontinuum optical frequency comb; FWs, filter wheels; PM, parabolic mirror; APD_{ref}, reference avalanche photodiode; P_2, rotating linear polarizer; APD_{prob}, probing avalanche photodiode; S, flip-in reflectance standard; T, target). (b) Schematic diagram of the experimental setup (P_1, linear polarizer; BS, beam sampler; M, mirror; FL, focusing lens).

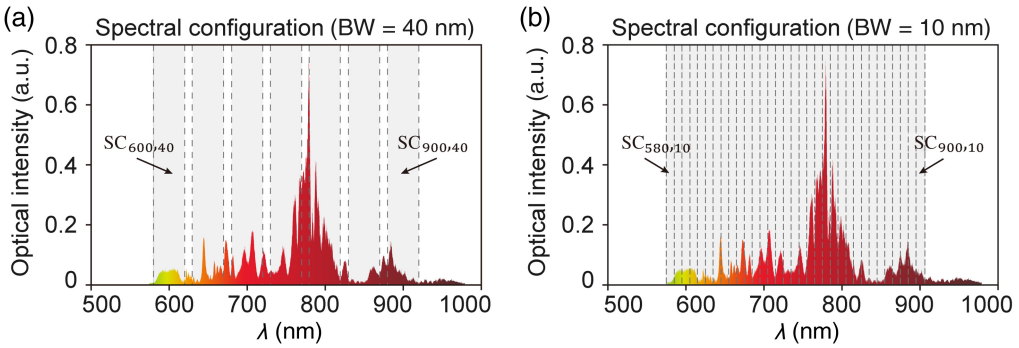

Fig. 2 Spectral configurations. The colorful area shows the optical spectral density of the supercontinuum optical frequency comb at different optical wavelengths λ. $SC_{a,b}$ denotes the spectral channel with a nm central wavelength and b nm spectral BW. (a) Spectral configuration with 40 nm BW. (b) Spectral configuration with 10 nm BW.

constitute one spectral configuration. Thirty-three band-pass filters with 10 nm BW and central wavelengths between 580 and 900 nm constitute the other spectral configuration.

According to the radar equation,[49,50] the reflectance R of a target can be expressed as a scaled ratio of the received optical power P_r and the transmitted optical power P_t of the LiDAR system as $R = K \cdot P_r/P_t$. The coefficient K is not a constant but depends on various parameters describing the measurement geometry (mainly incidence angle and ranging distance), atmospheric attenuation, and certain properties of the measurement system (e.g., aperture of the collection optics, wavelength of the laser, responsivity of the optical detector). The backscattered light detected by the probing APD yields a measure of the optical intensity I, which is proportional to P_r. We thus use the observed optical intensity as a proxy of the respective optical power in the rest of the paper.

The power of the supercontinuum laser source is unstable over periods of time longer than a few minutes.[51] We account for this along with all the parameters affecting K using time-multiplexed measurements (every 5 s) on a flip-in reflectance standard (Spectralon with 60% constant reflectance on the spectral range of interest). We estimate the reflectance of the target at a specific wavelength λ as

$$R(\lambda) = \eta_{\text{ratio}}(\lambda)\frac{I_{\text{T}}(\lambda)}{I_{\text{S}}(\lambda)}R_{\text{S}}, \tag{1}$$

where $R_{\text{S}} = 60\%$ is the known and constant reflectance of the reflectance standard, $\eta_{\text{ratio}}(\lambda) = K_{\text{T}}(\lambda)/K_{\text{S}}(\lambda)$ is the ratio of the parameters K which may be different for target and reflectance standard, if those are at different distance or viewed at different angles of incidence (AOI). $I_{\text{T}}(\lambda)$ and $I_{\text{S}}(\lambda)$ are the received optical intensities from the target and the reflectance standard, respectively. These optical intensities can be derived from the amplitudes A_{prob} of the electrical beat notes output by the probing APD and from the functional relationship $I = G(A_{\text{prob}})$. This function, as well as the determination of $\eta_{\text{ratio}}(\lambda)$, is explained in an earlier publication.[45] The reflectances measured in this way for the 7 and 33 spectral channels form the standard reflectance spectrum $R(\lambda)$ of the target for the 2 spectral configurations, respectively.

The polarimetric multispectral LiDAR[26] is adapted from the multispectral LiDAR prototype by setting a rotating linear polarizer (as analyzer) P_2 in front of the probing APD. The polarization direction of the backscattered light can then be analyzed by measuring the optical intensities at the probing APD as a function of the rotation of the analyzer. The additional polarization analyzer reduces the optical intensity detected by the probing APD by about 50%, which degrades the distance measurement precision with 1 ms integration time with respect to the 0.1 mm reported in our previous publication.[45] The distance precision including polarimetry is nevertheless still better than 0.2 mm for most spectral channels.

We configure the system such that the analyzer rotates to four directions in 45 deg steps. Without loss of generality, we use the first direction as reference direction and define it as 0 deg. Thus the four measured optical intensities are denoted by $I_{0\ \text{deg}}$, $I_{45\ \text{deg}}$, $I_{90\ \text{deg}}$, and $I_{135\ \text{deg}}$. The Stokes parameters (S_0, S_1, S_2, and S_3)[52] describe the polarization state of light. Since the laser source is linearly polarized and the backscattered light is only analyzed by a rotating linear polarizer in this setup, we can neglect S_3. According to the modified Pickering method,[52] the remaining Stokes parameters can be obtained from the optical intensities as

$$S_0 = \frac{I_{0\ \text{deg}} + I_{45\ \text{deg}} + I_{90\ \text{deg}} + I_{135\ \text{deg}}}{2}, \quad S_1 = I_{0\ \text{deg}} - I_{90\ \text{deg}}, \quad \text{and} \quad S_2 = I_{45\ \text{deg}} - I_{135\ \text{deg}}. \tag{2}$$

A more comprehensive understanding of the polarimetric characteristics of targets can be achieved by adding linear and circular polarization control at the emitter and receiver.[30,34,53,54] In this work, we only examine the linear polarization status at the receiver to decouple the impacts of surface roughness and material composition on the backscattered reflectance spectrum. For the sake of readability, references to polarimetric features in the remainder of the document thus represent only linear polarization characteristics even if not specified explicitly. The modified Pickering method was chosen herein for practical reasons prioritizing measurement precision over acquisition time.[52] In the case of applications with strong time requirements, the detection procedure for both the Pickering method and Fessenkov's method can be sped up by acquiring

intensities from only three analyzer angles while sacrificing measurement precision.[52,55] Further reducing to two analyzer angles is feasible through dual-polarization analysis, which is widely exploited in atmospheric polarimetric LiDAR.[28,29,56] This approach, however, requires a pre-alignment of the rotating analyzer to determine the co-polarization and cross-polarization directions. Given that 0 deg in $I_{0\ \mathrm{deg}}$ is the arbitrary reference direction of the rotating linear analyzer and not that of the co-polarization direction of backscattered light, the polarimetric analysis presented in this paper is not pre-aligned to determine the co-polarization and cross-polarization directions. The intensity measurement with the linear analyzer rotating at 45 deg and 135 deg is thus needed to determine the co-polarization direction, which we refer to as the angle of linear polarization (AoLP)[57] in this paper.

Based on these three Stokes parameters, the DoLP[57] and the AoLP within the interval $(-90\ \mathrm{deg}, 90\ \mathrm{deg}]$ can be calculated as

$$\mathrm{DoLP} = \frac{\sqrt{S_1^2 + S_2^2}}{S_0} \tag{3}$$

and

$$\mathrm{AoLP} = \frac{1}{2}\ \arctan\left(\frac{S_2}{S_1}\right). \tag{4}$$

The AoLP represents the angle between the polarization direction of the backscattered light and the reference direction of the linear polarizer. Using Malus' law,[57] we can express the four measured intensities as a function of the angle of the analyzer and of the linearly polarized and unpolarized components (I_{pol}, I_{unpol}) of the backscattered light:

$$I_{0\ \mathrm{deg}} = \cos^2(\mathrm{AoLP})I_{\mathrm{pol}} + \frac{1}{2}I_{\mathrm{unpol}}, \tag{5}$$

$$I_{45\ \mathrm{deg}} = \cos^2(45\ \mathrm{deg} - \mathrm{AoLP})I_{\mathrm{pol}} + \frac{1}{2}I_{\mathrm{unpol}}, \tag{6}$$

$$I_{90\ \mathrm{deg}} = \sin^2(\mathrm{AoLP})I_{\mathrm{pol}} + \frac{1}{2}I_{\mathrm{unpol}}, \tag{7}$$

$$I_{135\ \mathrm{deg}} = \sin^2(45\ \mathrm{deg} - \mathrm{AoLP})I_{\mathrm{pol}} + \frac{1}{2}I_{\mathrm{unpol}}. \tag{8}$$

According to Eqs. (5)–(8), the unpolarized and polarized intensities of the backscattered light can be derived as follows:

$$I_{\mathrm{unpol}} = \begin{cases} \dfrac{2\cos^2(\mathrm{AoLP})I_{90\ \mathrm{deg}} - 2\sin^2(\mathrm{AoLP})I_{0\ \mathrm{deg}}}{\cos^2(\mathrm{AoLP}) - \sin^2(\mathrm{AoLP})}, & \text{if } |\mathrm{AoLP}| \le 22.5\ \mathrm{deg} \\ & \text{or } 67.5\ \mathrm{deg} < |\mathrm{AoLP}| \le 90\ \mathrm{deg} \\ \dfrac{2\cos^2(\mathrm{AoLP} - 45\ \mathrm{deg})I_{135\ \mathrm{deg}} - 2\sin^2(\mathrm{AoLP} - 45\ \mathrm{deg})I_{45\ \mathrm{deg}}}{\cos^2(\mathrm{AoLP} - 45\ \mathrm{deg}) - \sin^2(\mathrm{AoLP} - 45\ \mathrm{deg})}, & \text{if } 22.5\ \mathrm{deg} < |\mathrm{AoLP}| \le 67.5\ \mathrm{deg}, \end{cases} \tag{9}$$

$$I_{\mathrm{pol}} = \begin{cases} \dfrac{I_{0\ \mathrm{deg}} - I_{90\ \mathrm{deg}}}{\cos^2(\mathrm{AoLP}) - \sin^2(\mathrm{AoLP})}, & \text{if } |\mathrm{AoLP}| \le 22.5\ \mathrm{deg} \\ & \text{or } 67.5\ \mathrm{deg} < |\mathrm{AoLP}| \le 90\ \mathrm{deg} \\ \dfrac{I_{45\ \mathrm{deg}} - I_{135\ \mathrm{deg}}}{\cos^2(\mathrm{AoLP} - 45\ \mathrm{deg}) - \sin^2(\mathrm{AoLP} - 45\ \mathrm{deg})}, & \text{if } 22.5\ \mathrm{deg} < |\mathrm{AoLP}| \le 67.5\ \mathrm{deg}. \end{cases} \tag{10}$$

The conditional functions given in Eqs. (9) and (10) are introduced to avoid values close to 0 in the denominator, which would amplify the uncertainty in the intensity measurements. Similarly to the definition of the standard reflectance spectrum $R(\lambda)$ given in Eq. (1), we introduce two quantities related to the unpolarized and linearly polarized intensities, determined for different wavelengths λ, and denote them herein as the unpolarized and polarized reflectances:

$$R_{\mathrm{unpol}}(\lambda) := \eta_{\mathrm{ratio}}(\lambda)\frac{I_{\mathrm{unpol,T}}(\lambda)}{I_{\mathrm{total,S}}(\lambda)}R_{\mathrm{S}}, \tag{11}$$

$$R_{\mathrm{pol}}(\lambda) := \eta_{\mathrm{ratio}}(\lambda)\frac{I_{\mathrm{pol,T}}(\lambda)}{I_{\mathrm{total,S}}(\lambda)}R_{\mathrm{S}}. \tag{12}$$

Here, $I_{\mathrm{total,S}}$ is the total intensity received from the reflectance standard and is equal to the first Stokes parameter $S_{0,\mathrm{S}}$ observed for the reflectance standard. The unpolarized and polarized reflectances measured in this way for different spectral channels form the unpolarized reflectance spectrum $R_{\mathrm{unpol}}(\lambda)$ and the polarized reflectance spectrum $R_{\mathrm{pol}}(\lambda)$ of the target.

3 Material Specimens and Data Collection

To indicatively analyze the performance of the polarimetric multispectral LiDAR in classifying material and surface roughness, we prepared two specimens of each of five materials, one for each of the two levels of surface roughness per material. The five materials are three types of plastic and two kinds of stone, namely polypropylene (PP), polyethylene (PE), polyvinyl chloride (PVC), limestone, and sandstone. The specimens were treated with an electric angle grinder and sandpaper suitable for plastics and stones with grit numbers P80 (rougher) and P400 (smoother), creating two clearly distinct surface roughness levels per material.

A picture of the 10 specimens is given in Fig. 3(a). The different surface roughness can be recognized in close-up photos obtained using a microscope [see Fig. 3(b)]. For the three plastic materials, the smoother surfaces (bottom row) can be characterized by a more homogeneous visual appearance, lower standard deviation of the surface height, and a smaller horizontal correlation length (defining "horizontal" as the mean orientation of the sample surfaces visible in the figure, and "height" as orthogonal to that direction). In contrast, a smoother surface for the stone materials (limestone and sandstone) means that the different mineral grains are exposed more clearly, thus leading to a visually more heterogeneous appearance. Although the same sandpaper is applied to all material specimens for a given surface roughness (P80 or P400), the surface morphology and thus final roughness are not the same for the different materials because of the different microstructure and densities. Herein, this is not a problem because we will restrict ourselves to distinguishing different levels of surface roughness. An extension of the approach to roughness quantification is left for future work.

For each specimen, we measured the reflectance spectrum $R(\lambda)$, unpolarized reflectance spectrum $R_{\mathrm{unpol}}(\lambda)$, and polarized reflectance spectrum $R_{\mathrm{pol}}(\lambda)$ at 20 different surface positions for both spectral configurations. This allows assessment of the uncertainty of the measurements resulting from measurement noise and from inhomogeneity across the surfaces. We then applied a linear SVM to classify different materials and roughness levels, and assessed the classification performance using cross-validation.[58]

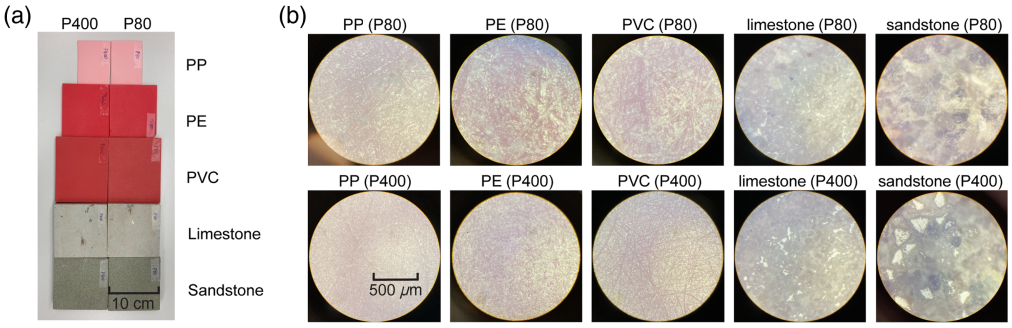

Fig. 3 Material specimens of five materials (PP, PE, PVC, limestone, and sandstone) in two levels of surface roughness (rough: P80; smooth: P400). (a) Picture of the material specimens. (b) Microscopic images of the material specimens with 100× magnification.

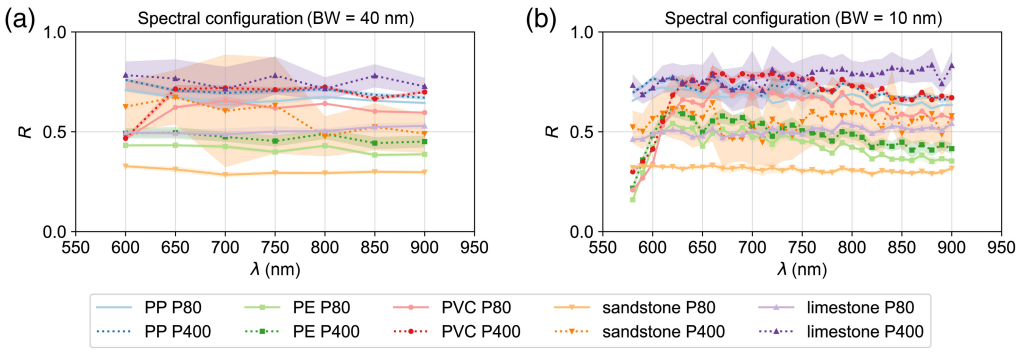

Fig. 4 Reflectance spectra $R(\lambda)$ of material specimens in (a) the spectral configuration with 40 nm BW and (b) the spectral configuration with 10 nm BW, where λ represents the central wavelength of each spectral channel. The lines represent the average values, and the shaded areas denote the standard deviations—note that the shaded areas are not visible for cases with comparatively small standard deviations. Different colors and markers represent different materials. Solid lines in lower color saturation and dotted lines in higher color saturation depict the two roughness levels, respectively.

4 Results

4.1 Multispectral Features

The reflectance spectrum $R(\lambda)$ (Fig. 4) represents multispectral features that could also be obtained using conventional multispectral LiDAR. The similarly red visual appearance of the chosen PE and PVC samples (see Fig. 3) is caused by pigments absorbing green and blue light. This is also indicated by the low reflectance for PE and PVC around 600 nm in the spectral signatures obtained using our prototypical LiDAR system, and demonstrates an obvious impact of the material on the features. To different extents, higher reflectance of the smoother surfaces (P400) compared to the rougher ones (P80) is apparent for all materials. The more heterogeneous surface of the smoother stone specimens (limestone and sandstone) leads to a significantly larger standard deviation because of the inhomogeneity across the surface. However, the reflectance spectra for the 10 specimens overlap with each other in the range of wavelengths provided by our setup, and independent classification of material and roughness does not seem possible using only these data in either spectral configuration.

4.2 Polarimetric Multispectral Features

The proposed polarimetric multispectral LiDAR provides different polarimetric multispectral features (see Fig. 5): the unpolarized reflectance spectrum $R_{\text{unpol}}(\lambda)$, the polarized reflectance spectrum $R_{\text{pol}}(\lambda)$, and the DoLP spectrum $\text{DoLP}(\lambda)$.

As shown in Figs. 5(a) and 5(b), $R_{\text{unpol}}(\lambda)$ of all specimens exhibits very low standard deviation. Specimens of the same material but different surface roughness have similar $R_{\text{unpol}}(\lambda)$, whereas specimens of different materials have significantly distinguishable $R_{\text{unpol}}(\lambda)$. This suggests that $R_{\text{unpol}}(\lambda)$ is largely independent of the surface roughness and depends mostly on the material itself. As discussed in Sec. 1, this can be explained by the volume scattering process affecting the light which penetrates into the material; this scattering causes depolarization and dominates $R_{\text{unpol}}(\lambda)$. The previously mentioned absorption-induced lower reflectance is very clearly indicated by R_{unpol} for PE and PVC between 580 and 620 nm in the spectral configuration with 10 nm BW and for PVC at 600 nm in the spectral configuration with 40 nm BW. In addition, all three plastic specimens (PP, PE, and PVC) also show a decrease in unpolarized reflectance from 800 to 900 nm for both spectral configurations. The very small standard deviation of $R_{\text{unpol}}(\lambda)$ shows that both spectral configurations provide good measurement precision for unpolarized reflectance over the investigated spectral range. The spectral configuration with 40 nm BW, however, exhibits fewer discriminative features than the spectral configuration with 10 nm BW in material distinction due to its lower spectral resolution (see, e.g., the spectral region around 600 nm).

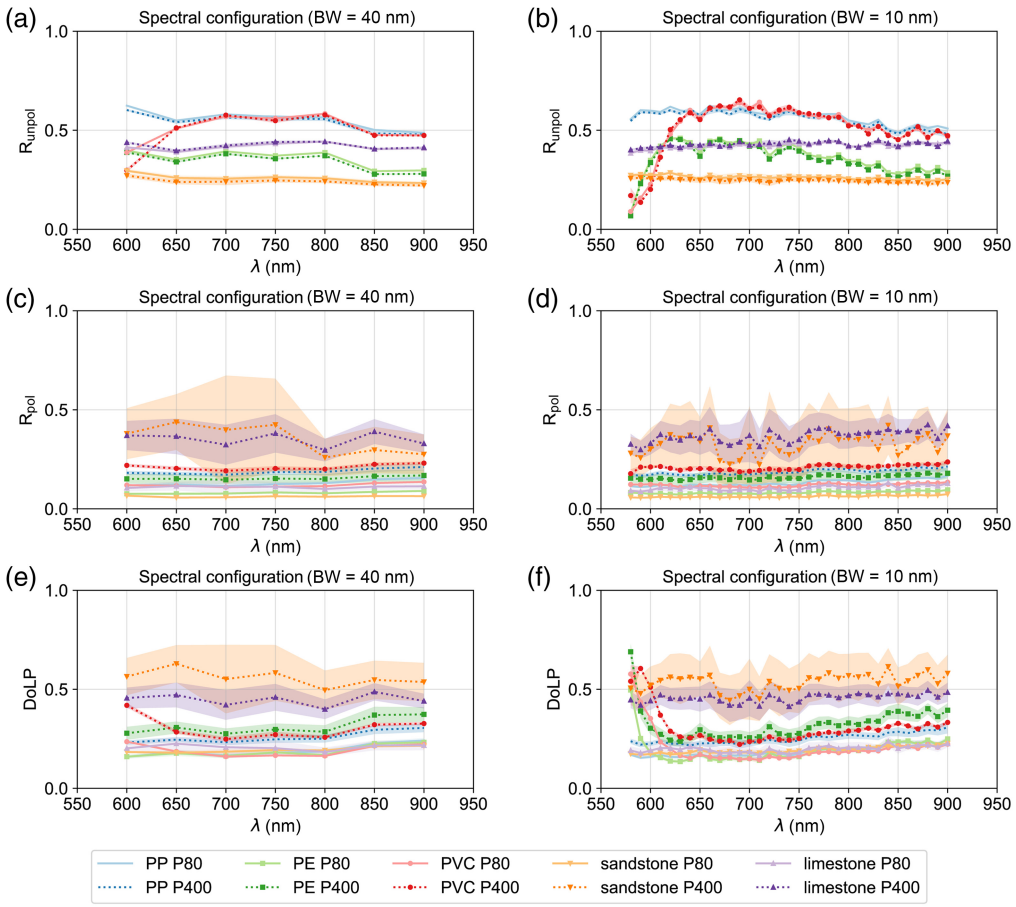

Fig. 5 Polarimetric spectra of material specimens, where λ represents the central wavelength of each spectral channel. Unpolarized reflectance spectra $R_{\text{unpol}}(\lambda)$ in (a) the spectral configuration with 40 nm BW and (b) the spectral configuration with 10 nm BW. Polarized reflectance spectra $R_{\text{pol}}(\lambda)$ in (c) the spectral configuration with 40 nm BW and (d) the spectral configuration with 10 nm BW. DoLP spectra DoLP(λ) in (e) the spectral configuration with 40 nm BW and (f) the spectral configuration with 10 nm BW. The lines represent the average values, and the shaded areas denote the standard deviations—note that the shaded areas are not visible for cases with comparatively small standard deviations. Different colors and markers represent different materials. Solid lines in lower color saturation and dotted lines in higher color saturation depict the two roughness levels, respectively.

As opposed to $R_{\text{unpol}}(\lambda)$, $R_{\text{pol}}(\lambda)$ exhibits significantly lower spectral dependency for both spectral configurations [see Figs. 5(c) and 5(d)]. This is due to R_{pol} being dominated by single and multiple reflections between surface microfacets. This mechanism is less affected by material-dependent absorption, and $R_{\text{pol}}(\lambda)$ thus shows less material-dependent signatures. Two reasons can explain the remaining apparent material dependence of $R_{\text{pol}}(\lambda)$: (1) according to the Fresnel equations,[59] the amount of reflection as opposed to transmission at the interface between two media depends on their refractive indices. (2) The treatment of the surfaces used herein may not actually result in the same roughness for different materials (see discussion in Sec. 3). However, for each material, $R_{\text{pol}}(\lambda)$ exhibits higher values for the smoother surfaces than for the rougher ones. Since smoother surfaces lead to narrower and stronger specular reflection lobes, the approximately normal incidence configuration of the setup (Fig. 1) causes the fixed aperture of the parabolic mirror to collect more polarization-preserved specularly reflected light, resulting in higher $R_{\text{pol}}(\lambda)$. For smoother stone specimens, the impact from the heterogeneous distribution of flat mineral grain surfaces is also visible in $R_{\text{pol}}(\lambda)$ through the much larger standard deviations. In summary, the results indicate that a smoother surface is associated with higher values of $R_{\text{pol}}(\lambda)$ than a rougher one. For the 10 specimens used herein, smooth and rough

samples have $R_{\mathrm{pol}}(\lambda)$ values differing by about 0.15 on average over the whole spectral range. As a result, surface roughness is one of the main drivers for distinguishable $R_{\mathrm{pol}}(\lambda)$, at least for AOI ≈ 0, making it a suitable proxy for roughness estimation. The dependence on AOI will have to be investigated in the future.

DoLP(λ), shown in Figs. 5(e) and 5(f), is a popular signature for distinguishing differences in specular reflection. The DoLP given by Eq. (3) describes the ratio of polarized intensity to total optical intensity. A highly-absorbing material can only reflect light from the surface as nearly all penetrated light is absorbed within the material, thus always leading to high DoLP with less dependency on the surface roughness. This can be demonstrated by the higher DoLP in the absorption region in the spectral configuration with 10 nm BW between 580 and 600 nm for the red PE and PVC with different surface roughness. Therefore, the DoLP(λ) of rougher PE and PVC overlaps with that of all the other smoother specimens between 580 and 600 nm, suggesting that the DoLP(λ) may be a slightly worse indicator for distinguishing different surface roughness than $R_{\mathrm{pol}}(\lambda)$.

4.3 Classification

As described in Sec. 3, we obtain 20 measurement samples from each material specimen. For the spectral configuration with 40 nm BW, each sample consists of a 28-dimensional feature vector composed of the 4 spectra $R(\lambda)$, $R_{\mathrm{pol}}(\lambda)$, $R_{\mathrm{unpol}}(\lambda)$, and DoLP$(\lambda)$ across seven spectral channels, whereas for the spectral configuration with 10 nm BW each sample consists of a 132-dimensional feature vector composed by the 4 spectra over 33 spectral channels. The entire dataset is well-balanced for both material and roughness classification. Each of the 5 material classes is represented by 40 samples, and each of the 2 surface roughness classes is represented by 100 samples. Although this dataset is small compared to the feature dimensionality, it enables a first indicative assessment of the benefit of the multispectral features for material and roughness classification. Herein, we will only analyze separate classification of material and of roughness and use only features of one type at a time. The feature vectors used for training and applying the SVM are therefore 7- and 33-dimensional subsets of the complete feature vectors for both spectral configurations, respectively.

To ensure that the training and testing data are as independent as possible and to obtain unbiased classification accuracy, we used twofold cross-validation for material classification and fivefold cross-validation for roughness classification. In each iteration of the twofold cross-validation for material classification, 100 samples obtained from 5 material classes and 1 roughness level were used as training data, and the other 100 measurement samples obtained from the same 5 material classes but from the other roughness levels were used for testing. For each iteration of the fivefold cross-validation of roughness classification, we used the 160 measurement samples from 4 material classes in both roughness levels for training and all 40 measurements of the remaining 2 specimens (i.e., same material but different roughness) for testing. We chose the same constant value of 0.1 for the regularization parameter of the linear SVM for all the classifications to simplify the comparison of the classification performance between different feature types.

The average and standard deviation of the material classification accuracies in the twofold cross-validation using the different features discussed above are listed in Table 1 for both spectral configurations. For material classification, $R_{\mathrm{unpol}}(\lambda)$ shows the highest average accuracy of 60% with a standard deviation of 0 in the spectral configuration with 40 nm BW and of 100% with a standard deviation of 0 in the spectral configuration with 10 nm BW. In fact, already Fig. 5(b) shows that the five materials can be perfectly distinguished in the spectral configuration with 10 nm BW, irrespective of the roughness class, using $R_{\mathrm{unpol}}(\lambda)$. The fewer discriminative features given by the spectral configuration with 40 nm BW [Fig. 5(a)] lead to a worse material classification performance than the spectral configuration with 10 nm BW.

Compared to the standard reflectance spectrum $R(\lambda)$, $R_{\mathrm{unpol}}(\lambda)$, only accessible by polarimetric multispectral LiDAR, can apparently improve the accuracy of classifying materials significantly. For the materials and datasets used here, the improvement is 25% and 59% for spectral configurations with lower and higher resolutions, respectively. In fact, the unpolarized reflectance spectra with the higher resolution allowed classifying all materials correctly, in our experiments.

Table 1 Material classification accuracy using different multispectral features provided by multispectral and polarimetric multispectral LiDAR in both spectral configurations. The average (mean) and standard deviation (std) of the classification accuracies are obtained from twofold cross-validations. The best classification performance among these multispectral features is listed in bold for each spectral configuration.

		Spectral configuration (BW = 40 nm)		Spectral configuration (BW = 10 nm)	
LiDAR	Features	Mean (%)	Std (%)	Mean (%)	Std (%)
Multispectral	$R(\lambda)$	48	8	63	1
Polarimetric multispectral	$R_{\text{unpol}}(\lambda)$	**60**	**0**	**100**	**0**
	$R_{\text{pol}}(\lambda)$	20	0	20	0
	DoLP(λ)	20	1	52	7

Material classification using only $R_{\text{pol}}(\lambda)$ (in both spectral configurations) or only DoLP(λ) (in the spectral configuration with 40 nm BW) seems to perform only as well as randomly guessing the material classes (accuracy of $20\% = 1/5$ with balanced samples from 5 classes). In fact, however, the standard deviation of 0 indicates that the classifier in these cases learns to output only one class label, irrespective of the spectral features. DoLP(λ) with the higher resolution spectrum (the spectral configuration with 10 nm BW) performs slightly better but still much worse than $R_{\text{unpol}}(\lambda)$. We conclude that $R_{\text{pol}}(\lambda)$ and DoLP(λ) are not sensitive enough to the materials themselves and thus not generally useful for material classification.

Table 2 summarizes the accuracies of roughness classification based on the fivefold cross-validation. For this classification task, $R_{\text{pol}}(\lambda)$ leads to the highest average accuracy of 92% with relatively small standard deviations of 15% and 11% for both spectral configurations, respectively. DoLP(λ) performs only slightly worse, which corresponds to the discussion in Sec. 4.2. $R(\lambda)$ seems to contain some information on surface roughness which leads to a classification accuracy slightly higher than random guessing, but much worse than using $R_{\text{pol}}(\lambda)$. Roughness classification using only $R_{\text{unpol}}(\lambda)$ does not work. The numbers in Table 2 show that the accuracy corresponds to that of random guessing and (with 0 standard deviation) the classifier just predicts constantly one of the two roughness classes for the spectral configuration with 10 nm BW, and it is only marginally better with the spectral configuration with 40 nm BW.

The concrete accuracies obtained herein are not yet generalizable because of the small dataset, both in terms of materials and roughnesses, as well as in terms of specimens per class. However, the results clearly indicate an advantage of polarimetric multispectral LiDAR as compared to standard multispectral LiDAR for classifying material and surface roughness. As

Table 2 Roughness classification accuracy using different multispectral features provided by multispectral and polarimetric multispectral LiDAR in two spectral configurations. The average (mean) and standard deviation (std) of the classification accuracies are obtained from fivefold cross-validations. The best classification performance among these multispectral features is listed in bold for both spectral configurations.

		Spectral configuration (BW = 40 nm)		Spectral configuration (BW = 10 nm)	
LiDAR	Features	Mean (%)	Std (%)	Mean (%)	Std (%)
Multispectral	$R(\lambda)$	66	20	60	12
Polarimetric multispectral	$R_{\text{unpol}}(\lambda)$	57	14	50	0
	$R_{\text{pol}}(\lambda)$	**92**	**15**	**92**	**11**
	DoLP(λ)	89	20	89	20

material classification requires more discriminative features to characterize the wavelength-dependent interaction between laser beam and surface material, the higher-resolution spectral configuration leads to better performance in material classification than the spectral configuration with a lower resolution in our experiments. Future investigations will be needed to find a good balance between small BW per channel for high spectral resolution and large bandwith per channel for better signal-to-noise ratio, faster data acquisition, and lower complexity of the measurement system. Oppositely, roughness classification seems to rely less on wavelength-dependent features. Both spectral configurations lead to a similar performance of roughness classification. A more comprehensive study further analyzing not only optimal spectral configurations but also combinations of feature types is needed. This requires a larger set of material samples and a variety of geometrical configurations, which will be enabled by further automation of the measurement process and by further development of the polarimetric multispectral LiDAR prototype toward a smaller form factor and transportability. These investigations are therefore left for future work.

5 Conclusion and Outlook

We presented an acquisition and analysis method for unpolarized and polarized reflectance spectra of natural surfaces using a novel polarimetric multispectral LiDAR to enhance remote sensing and classification of material and surface roughness. Data from 10 material specimens in 5 material classes and 2 levels of surface roughness were collected using our polarimetric multispectral LiDAR prototype. We introduced the polarized and unpolarized reflectance spectra and examined them in detail, comparing them to the standard reflectance spectrum.

The empirical results suggest that material composition and surface roughness are respectively the main drivers for the unpolarized and polarized reflectance spectra, which may therefore in turn be complementary features for classification and improve classification accuracy over the one attainable using standard multispectral data. In the present experimental investigation, we used two spectral configurations with different spectral resolutions but covering the same overall spectral range, and we applied a linear SVM for classification. In these experiments, the spectral resolution of 10 nm leads to better material classification than the 40 nm resolution, while there was practically no difference for roughness classification. The unpolarized reflectance spectrum with the higher resolution allowed to correctly classify the material among the five classes for all measurements (100% cross-validation accuracy). Material classification using a standard reflectance spectrum was substantially less accurate, and roughness classification using the standard spectrum was hardly better than random guessing.

Despite the small dataset available for these first tests, the results allow a proof of concept and clearly indicate the potential of the polarimetric multispectral LiDAR approach to enable much better material classification than standard multispectral LiDAR, as well as to open up the opportunity for deriving additional information on the surfaces from LiDAR data at the level of the individual measurement points, i.e., with high spatial resolution. In the future, it is important to generalize the findings presented herein, e.g., by extending the database of polarimetric spectral features by collecting data from a larger variety of specimens with different materials, different surface roughness, and at different distances and incidence angles.

Disclosures

The authors declare no conflicts of interest.

Code and Data Availability

Data and code underlying the results presented in this paper will be made publicly available in https://github.com/yuhan-yhyh/Dataset_Code_PML.git upon acceptance of this publication.

Acknowledgments

This research was partially funded by the Swiss National Science Foundation (Grant No. 200021_184988). The authors thank Robert Presl for helping prepare the material specimens,

Jingwen Li for her help in acquiring the microscopic images, and Jemil Avers Butt for discussing classification approaches. Parts of this work were presented at the SPIE Conference on Optical Metrology 2023, paper 126210D.[60]

References

1. I. H. Woodhouse et al., "A multispectral canopy LiDAR demonstrator project," *IEEE Geosci. Remote Sens. Lett.* **8**(5), 839–843 (2011).
2. B. Chen et al., "Hyperspectral LiDAR point cloud segmentation based on geometric and spectral information," *Opt. Express* **27**(17), 24043–24059 (2019).
3. J. Taher et al., "Feasibility of hyperspectral single photon LiDAR for robust autonomous vehicle perception," *Sensors* **22**(15), 5759 (2022).
4. S. Kaasalainen and T. Malkamäki, "Potential of active multispectral LiDAR for detecting low reflectance targets," *Opt. Express* **28**(2), 1408–1416 (2020).
5. J. Sun et al., "Evaluation of hyperspectral LiDAR for monitoring rice leaf nitrogen by comparison with multispectral LiDAR and passive spectrometer," *Sci. Rep.* **7**, 40362 (2017).
6. W. G. Rees, *Physical Principles of Remote Sensing*, Cambridge University Press (2013).
7. S. Kaasalainen et al., "Analysis of incidence angle and distance effects on terrestrial laser scanner intensity: search for correction methods," *Remote Sens.* **3**(10), 2207–2221 (2011).
8. R. Leach et al., "Interpreting the probe-surface interaction of surface measuring instruments, or what is a surface?" *Surf. Topogr. Metrol. Properties* **2**(3), 035001 (2014).
9. A. Townsend et al., "Surface texture metrology for metal additive manufacturing: a review," *Precis. Eng.* **46**, 34–47 (2016).
10. V. Frangez, D. Salido-Monzu, and A. Wieser, "Surface finish classification using depth camera data," *Autom. Constr.* **129**, 103799 (2021).
11. B. Zhang et al., "Impact of surface roughness, surface charge, and temperature on sandstone wettability alteration by nanoparticles," *Petrol. Sci.* **20**, 2852–2863 (2023).
12. R. Leach, *Optical Measurement of Surface Topography*, Vol. **8**, Springer (2011).
13. V. Badenko et al., "Scan-to-bim methodology adapted for different application," *Int. Arch. Photogramm. Remote Sens. Sp. Inf. Sci.* **42**, 1–7 (2019).
14. Z. Zahiri, D. F. Laefer, and A. Gowen, "Characterizing building materials using multispectral imagery and LiDAR intensity data," *J. Build. Eng.* **44**, 102603 (2021).
15. P. Tang et al., "Automatic reconstruction of as-built building information models from laser-scanned point clouds: a review of related techniques," *Autom. Constr.* **19**(7), 829–843 (2010).
16. Q. Lu and S. Lee, "Image-based technologies for constructing as-is building information models for existing buildings," *J. Comput. Civ. Eng.* **31**(4), 04017005 (2017).
17. M. Radanovic, K. Khoshelham, and C. Fraser, "Geometric accuracy and semantic richness in heritage BIM: a review," *Digit. Appl. Archaeol. Cult. Herit.* **19**, e00166 (2020).
18. M. Honic et al., "Framework for the assessment of the existing building stock through BIM and GIS," *Dev. Built Environ.* **13**, 100110 (2023).
19. E. Chuta, J. Colin, and J. Jeong, "The impact of the water-to-cement ratio on the surface morphology of cementitious materials," *J. Build. Eng.* **32**, 101716 (2020).
20. Z. Ge, Q. Sun, and N. Zhang, "Changes in surface roughness of sandstone after heating and cooling cycles," *Arab. J. Geosci.* **13**, 315 (2020).
21. N. Pfeifer et al., "Analysis of the backscattered energy in terrestrial laser scanning data," *Int. Arch. Photogramm. Remote Sens. Sp. Inf. Sci* **37**, 1045–1052 (2008).
22. D. Carrea et al., "Correction of terrestrial LiDAR intensity channel using Oren–Nayar reflectance model: an application to lithological differentiation," *ISPRS J. Photogramm. Remote Sens.* **113**, 17–29 (2016).
23. J. Bai et al., "A novel algorithm for leaf incidence angle effect correction of hyperspectral LiDAR," *IEEE Trans. Geosci. Remote Sens.* **60**, 1–9 (2022).
24. X. Li, L. Ma, and L. Xu, "Empirical modeling for non-Lambertian reflectance based on full-waveform laser detection," *Opt. Eng.* **52**(11), 116110 (2013).
25. E. Nunes-Pereira et al., "Polarization-coded material classification in automotive LiDAR aiming at safer autonomous driving implementations," *Appl. Opt.* **59**(8), 2530–2540 (2020).
26. Y. Han et al., "Polarimetric femtosecond-laser LiDAR for multispectral material probing," *Proc. SPIE* **12137**, 121370B (2022).
27. L. B. Wolff and T. E. Boult, "Constraining object features using a polarization reflectance model," *Phys. Based Vis. Princ. Pract. Radiom* **1**, 167 (1993).
28. R. M. Schotland, K. Sassen, and R. Stone, "Observations by LiDAR of linear depolarization ratios for hydrometeors," *J. Appl. Meteorol. Climatol.* **10**(5), 1011–1017 (1971).
29. K. Sassen, "The polarization LiDAR technique for cloud research: a review and current assessment," *Bull. Am. Meteorol. Soc.* **72**(12), 1848–1866 (1991).

30. B. V. Kaul, I. V. Samokhvalov, and S. N. Volkov, "Investigating particle orientation in cirrus clouds by measuring backscattering phase matrices with LiDAR," *Appl. Opt.* **43**(36), 6620–6628 (2004).
31. S. Burton et al., "Observations of the spectral dependence of linear particle depolarization ratio of aerosols using NASA Langley airborne high spectral resolution LiDAR," *Atmos. Chem. Phys.* **15**(23), 13453–13473 (2015).
32. L. Mei and P. Guan, "Development of an atmospheric polarization Scheimpflug LiDAR system based on a time-division multiplexing scheme," *Opt. Lett.* **42**(18), 3562–3565 (2017).
33. G. P. Kokhanenko et al., "Scanning polarization LiDAR LOSA-M3: opportunity for research of crystalline particle orientation in the ice clouds," *Atmos. Meas. Tech.* **13**(3), 1113–1127 (2020).
34. C. S. Chun and F. A. Sadjadi, "Polarimetric laser radar target classification," *Opt. Lett.* **30**(14), 1806–1808 (2005).
35. S. Guo et al., "Design and modeling of multi-spectral polarimetry streak tube imaging LiDAR," *Infrared Phys. Technol.* **118**, 103872 (2021).
36. S. Tan and R. M. Narayanan, "Design and performance of a multiwavelength airborne polarimetric LiDAR for vegetation remote sensing," *Appl. Opt.* **43**(11), 2360–2368 (2004).
37. S. Tan and A. Haider, "A comparative study of polarimetric and non-polarimetric LiDAR in deciduous-coniferous tree classification," in *IEEE Int. Geosci. Remote Sens. Symp.*, IEEE, pp. 1178–1181 (2010).
38. D. J. Harding, P. W. Dabney, and S. Valett, "Polarimetric, two-color, photon-counting laser altimeter measurements of forest canopy structure," *Proc. SPIE* **8286**, 828629 (2011).
39. S. Tan, S. Johnson, and Z. Gu, "Laser depolarization ratio measurement of corn leaves from the biochar and non-biochar applied plots," *Opt. Express* **26**(11), 14295–14306 (2018).
40. Y. Chen et al., "Detection and imaging of distant targets by near-infrared polarization single-pixel LiDAR," *Appl. Opt.* **61**(23), 6905–6914 (2022).
41. M. Ballesta-Garcia et al., "Analysis of the performance of a polarized LiDAR imager in fog," *Opt. Express* **30**(23), 41524–41540 (2022).
42. M. Alouini et al., "Near-infrared active polarimetric and multispectral laboratory demonstrator for target detection," *Appl. Opt.* **48**(8), 1610–1618 (2009).
43. S. Sattar et al., "Review of spectral and polarization imaging systems," *Proc. SPIE* **11351**, 113511Q (2020).
44. P. Ray et al., "Supercontinuum-based hyperspectral LiDAR for precision laser scanning," *Opt. Express* **31**, 33486–33499 (2023).
45. Y. Han, D. Salido-Monzú, and A. Wieser, "Comb-based multispectral LiDAR providing reflectance and distance spectra," *Opt. Express* **30**(23), 42362–42375 (2022).
46. C. Cortes and V. Vapnik, "Support-vector networks," *Mach. Learn.* **20**(3), 273–297 (1995).
47. F. Pedregosa et al., "Scikit-learn: machine learning in Python," *J. Mach. Learn. Res.* **12**, 2825–2830 (2011).
48. D. Salido-Monzú and A. Wieser, "An instrumental basis for multispectral LiDAR with spectrally-resolved distance measurements," *Int. Arch. Photogramm. Remote Sens. Sp. Inf. Sci.* **XLII-2/W13**(2/W13), 1121–1126 (2019).
49. A. V. Jelalian, *Laser Radar Systems*, Artech House on Demand (1992).
50. B. Höfle and N. Pfeifer, "Correction of laser scanning intensity data: data and model-driven approaches," *ISPRS J. Photogramm. Remote Sens.* **62**(6), 415–433 (2007).
51. P. Ray, D. Salido-Monzú, and A. Wieser, "High-precision intermode beating electro-optic distance measurement for mitigation of atmospheric delays," *J. Appl. Geodes.* **17**(2), 93–101 (2023).
52. J. R. Schott, *Fundamentals of Polarimetric Remote Sensing*, Vol. **81**, SPIE Press (2009).
53. C. J. Flynna et al., "Novel polarization-sensitive micropulse LiDAR measurement technique," *Opt. Express* **15**(6), 2785–2790 (2007).
54. M. Hayman et al., "Polarization LiDAR operation for measuring backscatter phase matrices of oriented scatterers," *Opt. Express* **20**(28), 29553–29567 (2012).
55. X. Wang et al., "Noise properties of the calculated linear polarization image," *Proc. SPIE* **10462**, 104622S (2017).
56. M. Haarig et al., "Triple-wavelength depolarization-ratio profiling of Saharan dust over Barbados during saltrace in 2013 and 2014," *Atmos. Chem. Phys.* **17**(17), 10767–10794 (2017).
57. E. Collett, *Field Guide to Polarization*, Field Guides, SPIE Press (2005).
58. R. Kohavi et al., "A study of cross-validation and bootstrap for accuracy estimation and model selection," in *IJCAI*, Montreal, Canada, Vol. 14, pp. 1137–1145 (1995).
59. B. E. Saleh and M. C. Teich, *Fundamentals of Photonics*, John Wiley & Sons (2019).
60. Y. Han, D. Salido-Monzú, and A. Wieser, "Classification of material and surface roughness using polarimetric multispectral LiDAR," *Proc. SPIE* **12621**, 126210D (2023).

Yu Han received her bachelor's degree from the University of Electronic Science and Technology of China and her master's degree from Karlsruhe Institute of Technology. Since October 2019, she has been working in the group of geosensors and engineering geodesy at

ETH Zürich as a scientific assistant and doctoral student. Her research interests are in investigating multimodal multispectral LiDAR based on a femtosecond laser supercontinuum to probe materials relevant for construction, structural monitoring, or geo-monitoring.

David Salido-Monzú is a senior scientist in the Institute of Geodesy and Photogrammetry at ETH Zürich, working also in sensor technology R&D in industry. His research interests include develop around optical metrology, electronic instrumentation, and signal processing, mainly applied to distance measurement, remote material probing, and sensing for electrification.

Andreas Wieser is a full professor of geosensors and engineering geodesy at ETH Zürich. He has more than 20 years of experience in academic research and teaching from various positions held at Vienna University of Technology, Graz University of Technology, and University of Calgary. He also worked in industry as a product manager for GPS-based tolling. His research interests include geodetic monitoring, digitization of reality, LiDAR, parameter estimation, and quality control.